BMC Genomics

RESEARCH

Open Access

Identification and functional validation of a novel *FBN1* variant in a Marfan syndrome family using a zebrafish model

Shitong Huang[1,2†], Jiansong Chen[2†], Qiuyu Wang[3†], Ruyue Zhang[4], Jian Zhuang[4,5], Ruiyuan Huang[1], Changjiang Yu[4], Miaoxian Fang[1], Haishan Zhao[5*] and Liming Lei[1,2,5*]

Abstract

Background Marfan syndrome (MFS) is an inherited autosomal dominant disorder that affects connective tissue with an incidence of about 1 in 5,000 to 10,000 people. 90% of MFS is caused by mutations in the fibrillin-1 (*FBN1*) gene. We recruited a family with MFS phenotype in South China and identified a novel variant. This study investigated whether this genetic variant is pathogenic and the potential pathway related to lipid metabolism in MFS.

Methods A three-generation consanguineous family was recruited for this study. Whole exome sequencing (WES) was utilized on family members. The 3D structure of the protein was predicted using AlphaFold. CRISPR/Cas9 was applied to generate a similar *fbn1* nonsense mutation (*fbn1*$^{+/-}$) in zebrafish. RNA-seq analysis on zebrafish was performed to identify potential pathways related to MFS pathogenesis.

Results Our study identified a novel variant [NM_000138.5; c.7764 C > G: p.(Y2588*)] in *FBN1* gene from the family and identified the same site mutation among the proband along with her son and daughter. Structural modeling showed the p.Y2588* mutation resulted from a truncated protein. Compared to wild-type zebrafish, the F2 generation *fbn1*$^{+/-}$ zebrafish exhibited MFS phenotype. RNA-seq analysis indicated that many genes related to leptin are up-regulating, which could affect bone development and adipose homeostasis.

Conclusion A novel variant was identified in FBN1 gene. In a zebrafish model, we found functional evidence supporting the pathogenicity of the detected nonsense mutation. Our research proposes a possible mechanism underlying the relationship between lipid metabolism and MFS. These findings can help improve the clinical diagnosis and treatment of MFS.

Keywords Marfan syndrome, FBN1, Novel pathogenic variant, Nonsense mutation, Zebrafish, Lipid metabolism

†Shitong Huang, Jiansong Chen and Qiuyu Wang contributed equally to this work.

*Correspondence:
Haishan Zhao
hartzhao@163.com
Liming Lei
leiliming@gdph.org.cn
[1]Department of Cardiac Surgical Intensive Care Unit, Guangdong Cardiovascular Institute, Guangdong Provincial People's Hospital (Guangdong Academy of Medical Sciences), Southern Medical University, Guangzhou 510080, China
[2]Department of Cardiovascular Surgery, Guangdong Provincial People's Hospital's Nanhai Hospital, The Second People's Hospital of Nanhai District Foshan City, Foshan, Guangdong 528200, China
[3]Department of Cardiac Surgical Intensive Care Unit, Guangdong Provincial People's Hospital (Guangdong Academy of Medical Sciences), Southern Medical University, Guangzhou 510080, China
[4]Department of Cardiovascular Surgery, Guangdong Cardiovascular Institute, Guangdong Provincial People's Hospital (Guangdong Academy of Medical Sciences), Southern Medical University, Guangzhou 510080, China
[5]Guangdong Provincial Key Laboratory of South China Structural Heart Disease, Guangdong Cardiovascular Institute, Guangdong Provincial People's Hospital (Guangdong Academy of Medical Sciences), Southern Medical University, Guangzhou 510080, China

Introduction

Marfan syndrome (MFS), an inherited autosomal dominant condition, affects the connective tissue and occurs in approximately 1 in every 5,000 to 10,000 individuals [1]. MFS presents with a spectrum of signs and symptoms that can vary widely. The condition predominantly affects the skeletal, cardiovascular, and ocular systems, although the impact extends to all fibrous connective tissues throughout the body. The most significant health risks are associated with the dilation and dissection of the ascending aorta, which are the primary causes of morbidity and mortality in MFS patients. Additionally, certain individuals with MFS may exhibit a pronounced deficiency in subcutaneous adipose tissue, leading to an unusually slender physical appearance.

Fibrillin-1, encoded by the *FBN1* gene, is a large extracellular matrix glycoprotein rich in cysteine and capable of calcium binding. It functions as a key structural element of microfibrils, offering essential mechanical support in both elastic and non-elastic connective tissues. Multiple gene loci related to MFS have been discovered, of which *FBN1* is the most critical gene [2]. Over 3000 MFS patients have been identified with more than 1800 pathogenic variants in the *FBN1* gene, with missense mutations being the most prevalent, succeeded by nonsense mutations and minor insertions or deletions [3].

According to the NCBI database, 310 organisms have orthologs with the human *FBN1* gene, including mice, rats, pigs, and zebrafish [4]. Sequencing studies in zebrafish have uncovered that around 70% of human genes possess functional counterparts in this species. Lately, the CRISPR/Cas9 genome-editing technology has made significant strides and is being utilized in zebrafish to modify gene transcription and function [5, 6]. Given the genetic similarities between humans and zebrafish, as well as the powerful genome editing tools available, zebrafish represent an ideal model system for genetic research on Marfan syndrome.

In this study, we report on a female patient clinically diagnosed with MFS who exhibited typical MFS characteristics and aberrant right subclavian artery. Whole Exome Sequencing (WES) was performed on four members of the patient's family to identify the causal variant for MFS. We discovered an exonic variant of the *FBN1* gene (c.7764 C > G) in the proband, her daughter, and her son. AlphaFold is an artificial intelligence system designed to predict the structure of protein [7]. The pathogenicity of this FBN1 variant was verified through computer prediction and functional studies. We generated a transgenic line of $fbn1^{+/-}$ zebrafish by CRISPR/Cas9 system and studied the phenotype in $fbn1^{+/-}$ zebrafish. Additionally, we conducted RNA sequencing on zebrafish models to analyze potential differential genes associated with MFS and subsequently validated them using RT-qPCR and Western blotting.

Methods

Patients and clinical data

In this study, we enrolled a three-generation consanguineous family. We conducted home visits to gather clinical data and family history through interviews. With the consent of each participant, we collected peripheral blood samples from both affected and unaffected family members. The study was approved by the Institutional Review Board of Guangdong Provincial People's Hospital.

Affected family members underwent clinical assessments by certified clinicians and cardiologists, who utilized family history, symptoms, and medical records to establish a diagnosis. Upon admission, patients underwent a series of diagnostic imaging and tests, including computed tomography angiography (CTA), transthoracic echocardiography (TTE), and electrocardiogram (ECG), to ascertain an MFS diagnosis. Concurrently, blood and urine samples were collected for laboratory analysis. The systemic features of MFS were scored using the revised Ghent nosology. Additionally, their offsprings underwent physical examinations, TTE, and computed tomography (CT) scans to assess their likelihood of an MFS diagnosis.

DNA isolation and whole exome sequencing

Constitutional DNA was extracted from peripheral blood using standard protocols, involving phenol-chloroform extraction and ethanol precipitation methods. Genomic DNA of 1–3 μg was fragmented to an average size of 150 bp using a S220 Focused-ultrasonicator (Covaris, Massachusetts, USA). A DNA Sample Prep Reagent Set (MyGenostics, Beijing, China) was used for the preparation of standard Illumina libraries, including end repair, adapter ligation, and PCR amplification, which would be further sequenced by DNBSEQ (DNBSEQ-T7).

After sequencing, the raw data were saved as a FASTQ format. Both Illumina sequencing adapters and low quality reads (< 80 bp) were filtered by cutadaptor software (http://code.google.com/p/cutadapt/). The clean reads were mapped to the UCSC hg19 human reference genome using the parameter BWA of Sentieon software.(https://www.sentieon.com/). The duplicated reads were removed using the parameter driver of Sentieon software, and the parameter driver is used to correct the base, so that the quality value of the base in the reads of the final output BAM file can be closer to the real probability of mismatch with the

reference genome, and the mapped reads were used for the detection of variation. The variants of SNP and InDel were detected by the parameter driver of Sentieon software. Then, the data would be transformed to VCF format. Variants were further annotated by ANNOVAR software (http://annovar.openbioinformatics.org/en/latest/), and associated with multiple databases, such as, 1000 genome, ESP6500, dbSNP, EXAC, Inhouse (MyGenostics), HGMD, and also predicted by SIFT, PolyPhen-2, MutationTaster, GERP++.

In this study, four steps were used to select the potential pathogenic mutations in downstream analysis: (i) Mutation reads should be more than 5, and mutation rate should be no less than 30%; (ii) The mutations should be removed, when the frequency of mutation was more than 5% in 1000G, ESP6500, and Inhouse database; (iii) The mutations should be dropped, if they were in InNormal database (MyGenostics); (iV) The synonymous mutations should be removed, when they were not in the HGMD database. After that, the rest mutations should be the potential pathogenic mutations for further analysis. Evaluation of variant pathogenicity was performed using standards and guidelines from the American College of Medical Genetics and Genomics (ACMG) [8].

Homology modeling and function prediction

The amino acid sequence was retrieved from the UniProt database [9] and formatted into a FASTA file. The protein of FBN1 was deconstructed into three segments. AlphaFold used the known FBN1 sequence to predict the 3D structure of the protein by searching for proteins with known structures homologous to the sequence in the protein database [10]. Through the homology modeling software MODELLER 9.15, a script salign.py is written to compare the target sequence with the template sequence. After sequence alignment, upload the coordinate file of the template protein, write a script model_mult.py, and run the script to construct the protein model. The quality of the predicted model was assessed using MolProbity, ensuring that it met the standards for protein geometry. The final structure was analyzed to elucidate potential functional sites and binding motifs [11].

Zebrafish care and husbandry

Transgenic Tg (kdrl: EGFP) and Tg (myl: EGFP) zebrafish possessing a green fluorescent heart [12] were obtained from the China zebrafish resource center (Wuhan Hubei, China). These two transgenic zebrafish models exhibit green fluorescence in their blood vessels and heart, respectively. The fish were housed in a zebrafish recirculating breeding system, maintained at a temperature of 26 ± 2℃ with a 14-hour light and 10-hour dark photoperiod. For reproduction, mating was conducted at an equal 1:1 ratio, allowing for natural spawning to occur.

Generation of Cas9 Transgenic zebrafish

A novel pathogenic variant [NM_000138.5; c.7764 C > G: p.(Y2588*)] was identified in *FBN1* gene by carrying out WES for the proband, her son and daughter, and her husband. In the NCBI database (https://www.ncbi.nlm.nih.gov/gene/XM_017351990.2), the 7764 locus of the human *FBN1* gene corresponded to the 2588 locus of the zebrafish *fbn1* gene, and this design is based on the NCBI database. *fbn1* sgRNAs (CRISPR1: GGGTATCTGTGCTCCTGTCC ACGCGG; CRISPR2: GGTATCTGTGCTCCTGTC CACGCGG; CRISPR3: GTATCTGTGCTCCTGTCC ACGCGG) were designed and synthesized by Shanghai Generay Biotech Co., Ltd. The target sequences are in exon 19. A mixture consisting of 1 nl of each sgRNA (concentrated at 80–100 ng/μl) and Cas9 protein was precisely injected into the F0 embryos. These injected F0 embryos were nurtured until they reached sexual maturity, after which eight pairs of mature adult zebrafish were bred to generate F1 generation embryos for subsequent analysis.

Genotyping of Transgenic zebrafish

Genomic DNA was obtained by alkaline lysis method from F1 embryos at 24 hours post-fertilization (hpf). Performing PCR amplification of genomic DNA using forward (5'-ACACAGCTGTATCTCAAGTGTT-3') and reverse (5'-GTGTGTTTTACCTCTGCAGCTC-3') primers in thermal cycler (Thermo Fisher, Shanghai, China) to determine the genotype. The PCR protocol initiated with a denaturation step at 95 °C for 3 min, followed by 35 cycles of denaturation at 95 °C for 15 s, annealing at 60 °C for 30 s, and extension at 72 °C for 12 s, with a final extension at 72 °C for 5 min to complete the process. The PCR reaction was conducted utilizing the aforementioned primers and PCR protocol. To confirm the genotype carried by the mutants, the PCR amplicons were recombined into the pEASY-T3 Cloning vector (CT301, Transgen, Beijing, China). Following the transformation process, a singular bacterial colony was carefully selected for subsequent DNA sequencing. F0 individuals harboring heritable mutations were chosen to breed with Tg(kdrl: EGFP) and Tg(myl: EGFP) zebrafish lines to produce F1 progeny. Genomic DNA was extracted at two months post-fertilization for genotyping, and the identified F1 $fbn1^{+/-}$ heterozygotes were utilized in subsequent studies. Adult F1 $fbn1^{+/-}$ zebrafish were then interbred to generate F2 transgenic offspring for further investigation.

Morphology assessment

The morphology of F2 embryos/larvae and wild-type (WT) control group were subsequently fixed on glass slides with 4% methylcellulose (Yuanye, Shanghai, China), and the cardiovascular phenotype was recorded by employing an upright microscope (Axio Lab. A1, Carl Zeiss, Germany). Dorsal and ventral view image data were imported into the ImageJ software (version, V1.53q). The initial sample size for both the F2 *fbn1*$^{+/-}$ zebrafish experimental group and the WT control group was 743. Statistical analysis was conducted to compare the abnormal phenotypes between the F2 and WT groups. The experiment was conducted thrice to ensure reliability. Statistical analysis was performed using SPSS 22.0 software, with significance set at $p < 0.05$. A Chi-square test was utilized to evaluate the data regarding abnormal angiogenesis phenotypes in both the F2 and WT groups at 120 hpf. In this study, a total of 743 animals were used across three independent experiments. Specifically, the first experiment included 240 animals, the second experiment included 249 animals, and the third experiment included 254 animals.

Whole-mount Alcian blue staining

Zebrafish larvae at 144 hpf WT and *fbn1*$^{+/-}$ zebrafish were processed for the visualization of bone and cartilage using Alcian Blue 8GX (Solarbio, Beijing, China). Initially, the larvae were fixed in 2% paraformaldehyde for 2 h with gentle rocking. Subsequently, they were stained in an acid-free, double-stain solution containing 120 mM $MgCl_2$ overnight, which provides superior differentiation of cartilaginous and osseous structures compared to acidic conditions. After staining, the larvae were bleached with 3% hydrogen peroxide (H_2O_2) for 25 min, followed by treatment with 1% potassium hydroxide (KOH). The specimens were then dehydrated with 20% glycerol and 0.25% KOH overnight, with a subsequent increase to 50% glycerol and 0.25% KOH for a second overnight incubation. Finally, the prepared samples were stored in a solution of 50% glycerol and 0.1% KOH at 4 °C. The cartilaginous phenotype was recorded by employing an upright microscope (Axio Lab. A1, Carl Zeiss, Germany). Ventral view image data were imported into the ImageJ software (version, V1.53q).

RNA isolation, cDNA library preparation, and RNA sequencing (RNA-Seq)

Total RNA was extracted from 120 hpf *fbn1*+/- zebrafish and WT zebrafish embryos by utilizing the Total RNA Isolation Kit (RC101, Vazyme, Nanjing, China), according to the manufacturer's protocol. Assays of total RNA quality were carried out on an Agilent 2100 Bioanalyzer (Agilent, CA, USA), agarose gel electrophoresis, and nanophotometer. The first strand of cDNA was synthesized utilizing the M-MuLV reverse transcriptase system, with fragmented mRNA serving as the template and a random oligonucleotide as the primer. Following this, the RNA strand was degraded using RNaseH. Subsequently, the second strand of cDNA was synthesized from dNTPs with the aid of the DNA polymerase I system. The purified double-stranded cDNA underwent end repair, a tail, and ligation of sequencing adaptors to finally establish 12 cDNA libraries consisting of three repeats in each set and were sequenced in paired-end 150 bp mode using the Illumina HiseqTM 2500/4000 platform. RNA library sequencing was assisted by Gene Denovo Biotechnology, Ltd (Guangzhou, China).

Global and differential gene expression analysis

Differential gene expression analysis was performed utilizing the DESeq228 software package, identifying differentially expressed genes (DEGs) with a fold change threshold of greater than 1.5 and a *p*-value cutoff of less than 0.05. The biological functions of these significantly expressed genes were categorized based on annotations from the Kyoto Encyclopedia of Genes and Genomes (KEGG) database and the Gene Ontology (GO) consortium. GO terms and KEGG pathways with a *p*-value below 0.05 were deemed to be significantly enriched and thus considered in the analysis.

Real-time quantitative PCR (RT-qPCR)

Total RNA was extracted from 120 hpf *fbn1*+/- zebrafish and WT zebrafish embryos by utilizing the Total RNA Isolation Kit (RC101, Vazyme, Nanjing, China), according to the manufacturer's protocol. Complementary DNA (cDNA) was synthesized from 1 μg of total RNA using the High-Capacity cDNA Reverse Transcription Kit (EZ Bioscience) in a 20 μL reaction volume. The reaction conditions were 25 °C for 10 min, followed by 37 °C for 120 min, and finally 85 °C for 5 min. The cDNA was diluted to a final concentration of 10 ng/μL with nuclease-free water and stored at -20 °C until use. qPCR was performed using SYBR Green PCR Master Mix (EZ Bioscience) on an Applied Biosystems 7500 Real-Time PCR System. Each 20 μL reaction contained 10 μL of SYBR Green Master Mix, 2 μL of cDNA, and 200 nM of each primer. The cycling conditions were 95 °C for 10 min, followed by 40 cycles of 95 °C for 15 s, and 60 °C for 1 min. A melting curve analysis was performed to confirm the specificity of the amplification. The relative expression levels were calculated using the 2^-ΔΔCT^ method.

Zebrafish protein extraction and Western blot analysis

At 120 hpf, both WT and F2 *fbn1*$^{+/-}$ zebrafish were swiftly dissected and flash-frozen in liquid nitrogen. Subsequently, tissue samples were homogenized in Radio-Immunoprecipitation Assay (RIPA) buffer, which consists of 50 mM Tris-HCl at pH 7.4, 150 mM NaCl, 1% NP-40, 0.5% sodium deoxycholate, 0.1% SDS, and a mixture of protease inhibitors (Roche Complete Mini, EDTA-free). Lysates were sonicated on ice to shear DNA and further homogenized using a polytron homogenizer. Following a 30-minute incubation on ice, the lysates were centrifuged at 14,000 rpm for 15 min at 4 °C to sediment the debris. The supernatant was then carefully collected, and the protein concentration was measured using the BCA protein assay kit (Thermo Fisher Scientific).

Protein samples (30 μg per lane) were mixed with loading buffer (Absin, Shanghai, China) and boiled for 5 min at 95 °C. Proteins were resolved via SDS-PAGE on a 10% polyacrylamide gel and subsequently transferred onto a nitrocellulose membrane. This membrane was then blocked with a solution containing 5% non-fat dry milk in Tris-buffered saline with 0.1% Tween-20 (TBST) for 1 h at ambient temperature. The primary antibodies were diluted in TBST with 5% bovine serum albumin (BSA) and incubated with the membrane overnight at 4 °C. After washing with TBST, the membrane was incubated with horseradish peroxidase-conjugated secondary antibodies for 1 h at room temperature. After additional washing steps, protein bands were revealed using an enhanced chemiluminescence (ECL) detection system. The intensities of these bands were subsequently quantified employing ImageJ software.

Ethical compliance and ethical considerations

All procedures performed in studies involving human participants were in accordance with the ethical standards of the institutional and/or national research committee and with the 1964 Helsinki declaration and its later amendments or comparable ethical standards. Informed consent was obtained from all individual participants included in the study. All animal experiments were conducted in accordance with the guidelines of the Guangdong Provincial People's Hospital Animal Care and Use Committee and were approved under the ethical approval number KY2023-519-02. The guidelines from Directive 2010/63/EU of the European Parliament on the protection of animals used for scientific purposes and the NIH Guide for the Care and Use of Laboratory Animals were strictly followed to ensure the welfare of the animals.

Ethics statement

This article adhered to the ethical guidelines for research and publication as outlined by the Guangdong Provincial People's Hospital. Formal written consent was obtained from all individual participants for the publication of images in Fig. 1a and b.

Results

Family recruitment and clinical presentation

A 33-year-old female was admitted with a 4-year history of shortness of breath and heart palpitations. Physical examination revealed that the patient was 155 cm tall and exhibited Marfanoid features, including scoliosis, slender limbs, and spider toes (Fig. 1A). The three-dimensional (3D) reconstructions of the spine and aorta also revealed scoliosis, Stanford type A aortic dissection, aortic coarctation, and aberrant right subclavian artery in the patient (Fig. 1B). The patient had an elder brother and two elder sisters. Her father had passed away suddenly in his thirties. The patient is the mother of two children: a 9-year-old boy and an 11-year-old girl. According to the growth and development reference standards for Chinese children published by the National Health Commission of China, the 97th percentile (P97) for a 9-year-old boy is 153.3 cm. For an 11-year-old girl, the P97 is 159.2 cm. Notably, the heights of her son and daughter are 158 cm and 172 cm, respectively. These values are significantly higher than the average heights for children of the same age in China, placing them well above the 97th percentile for their respective age and sex groups. And they presented with scoliosis, high myopia, and slender limbs, suggesting a familial pattern of Marfan syndrome. The family was interviewed (Fig. 1C), and peripheral blood samples were collected for further genetic analysis after obtaining informed consent and approval from the Institutional Review Boards (IRB).

Identification of a novel *FBN1* mutation

WES was performed on the proband, her son and daughter, and her husband. The identified genetic variant was subsequently validated using Sanger sequencing in all other family members. A novel variant [NM_000138.5; c.7764 C > G: p.(Y2588*)] was identified in the *FBN1* gene and evaluated for segregation within the family (Fig. 2A). This new variant located in coding exon 63 of the *FBN1* gene, results from a C to G substitution at nucleotide position 7764. Sanger sequencing did not detect the same mutation in other family members (Fig. 2B), suggesting that the patient's variant is a de novo mutation that has been inherited to her son (III-1) and daughter (III-2) (Fig. 1C), they are now receiving medical treatment and follow-up care. The variant is classified as Likely Pathogenic

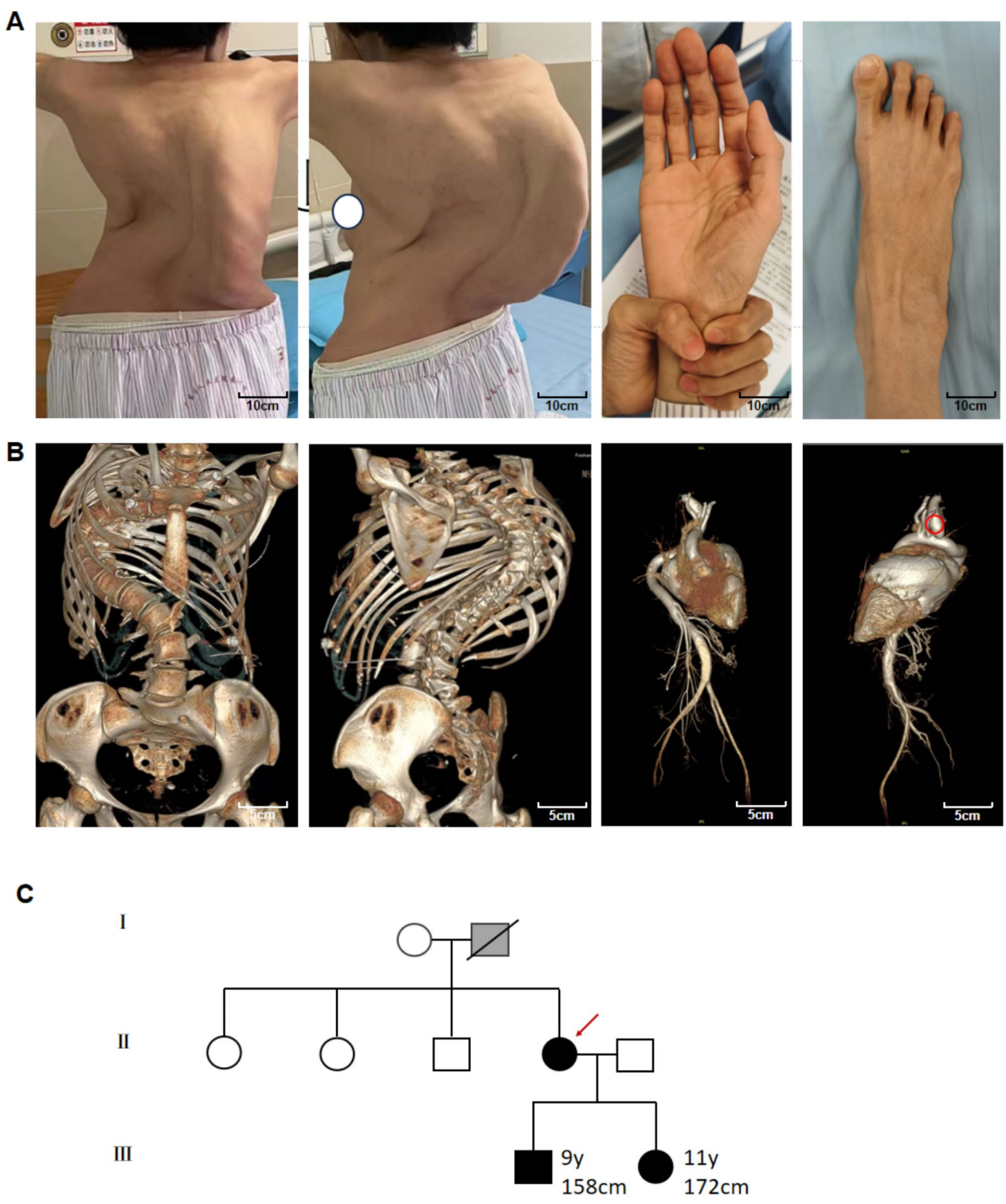

Fig. 1 Marfanoid symptoms of the patient. (**A**) Clinical manifestations of the spine, hands, and feet. (**B**) CT three-dimensional (3D) reconstructions of the spine and aorta. These reconstructions revealed "scoliosis" and "Stanford type A aortic dissection, aortic coarctation, and aberrant right subclavian artery". The red circle indicated the right subclavian artery of ectopic origin. (**C**) Family pedigree. The red arrow indicates the proband. Blank filling indicates not affected, black filling indicates affected and genetically confirmed, and green filling indicates affected but not genetically tested. A line through the shape indicates the dead member

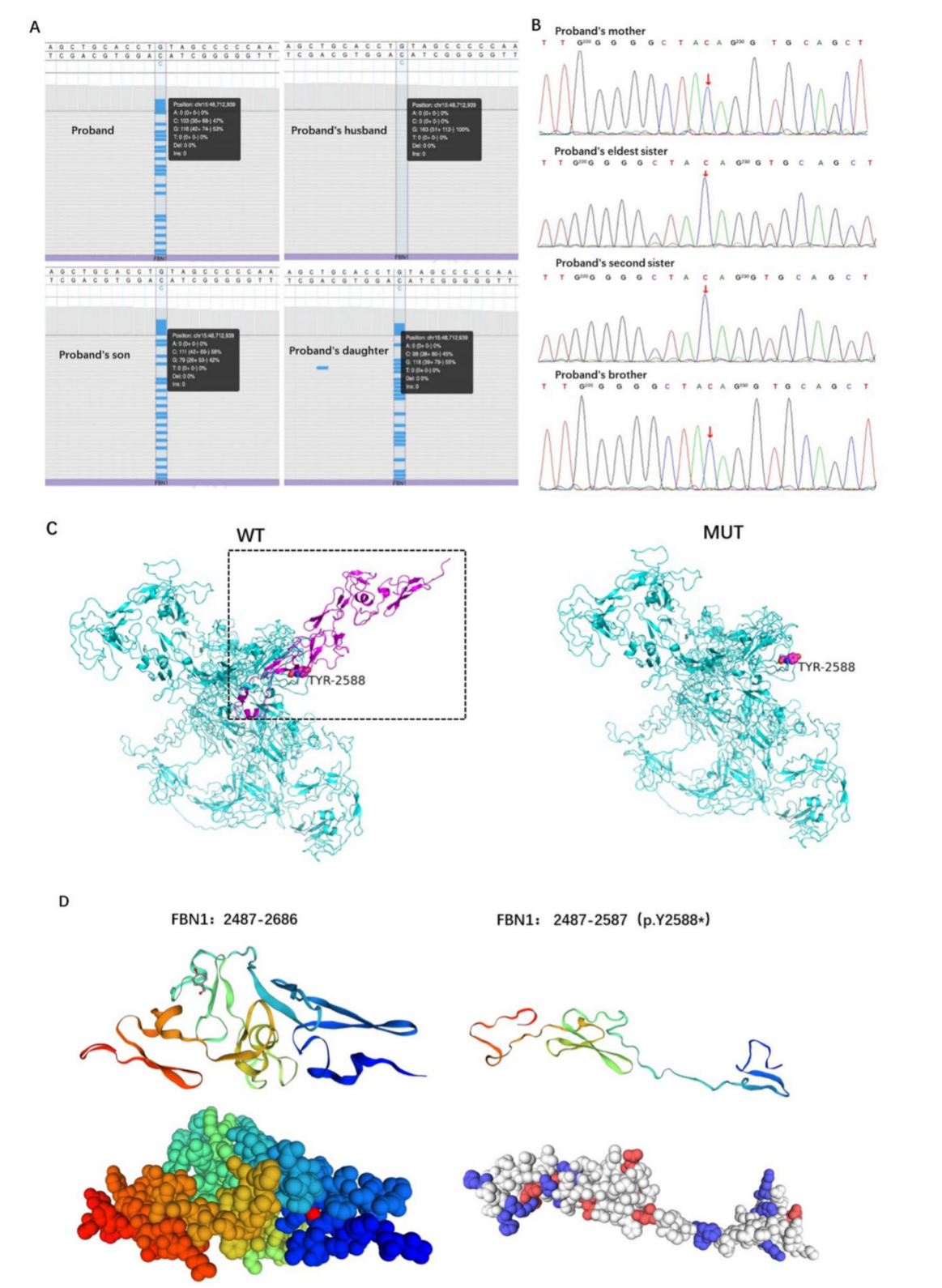

Fig. 2 (See legend on next page.)

(See figure on previous page.)

Fig. 2 WES identified a novel *FBN1* mutation [NM_000138.5; c.7764 C > G: p.(Y2588*)] and thestructural reconstruction. (**A**). BAM illustration of WES in the proband's family of four. The gray area indicated the second-generation capture coverage. At position c.7764, the C/G ratio is as follows: C: 103 (forward: 35 +, reverse: 68 -), comprising 47% of the total; G: 116 (forward: 42 +, reverse: 74 -), comprising 53% of the total. (**B**). The Sanger sequence of other 4 family members showed no mutation in c.7764. (**C**). Protein prediction models of WT FBN1 and p.Y2588* mutated FBN1. The p.Y2588* mutation leads to the substitution of the 2588th amino acid of the wild-type FBN1 protein with a premature stop codon, resulting in an FBN1 protein with only 2588 amino acids, thereby lacking 283 amino acids. (**D**). Structural models for the wild-type and mutant FBN1 proteins in 2487aa-2686aa region. The p.Y2588* variant also led to a more loosely arranged and structurally abnormal conformation in the 2487aa-2588aa region of the protein, prior to the premature termination

(LP) based on ACMG criteria (PS3, PM2,PM6), this variant is not observed in population databases, such as gnomAD. This absence from population databases strengthens the argument for its potential pathogenicity.

Potential consequences of the mutation and FBN1 protein model predicting

The p.Y2588* mutation resides in the 31st calcium-binding EGF-like (cbEGF) domain (Fig. 3A), where it causes the entire protein to comprise only 2588 amino acids. This results in the absence of 283 amino acids. Specifically in terms of structure, the C-terminal of FBN1 lacks 283 amino acids, leading to the deficiency of 17 β-folded structures, 4 α-helix structures, and various loop structures (Fig. 2C).

Using the 2487aa-2686aa region of the FBN1 protein as a template with online Swiss-Model (https://swissmodel.expasy.org/), we predicted the structural models for the WT and mutant FBN1 proteins. We found that in addition to the premature termination and the loss of the C-terminal 283 amino acids, the p.(Y2588*) variant also led to a more loosely arranged and structurally abnormal conformation in the 2487aa-2588aa region of the protein, prior to the premature termination (Fig. 2D).

Generation of *fbn1*$^{+/-}$ zebrafish

Comparative analyses using NCBI and Ensembl resources revealed that the *FBN1* gene is orthologous between humans and zebrafish (Fig. 3A), indicating that zebrafish is a suitable model organism for genetic research on *FBN1* mutations. The p.Y2588* mutation resides in the 31st calcium-binding EGF-like domain (Fig. 3A), which corresponds to the 19th calcium-binding EGF-like domain in the zebrafish *fbn1* gene (Fig. 3B). To generate an fbn1 mutant zebrafish model, we designed three single-guide RNAs (sgRNAs) targeting exon 28 of the zebrafish *fbn1* gene and tested their efficiency by co-injecting them with Cas9 protein into one-cell stage zebrafish embryos. DNA sequencing of the target-specific PCR products confirmed that the edited fbn1 allele contained several nucleotide deletions and a 4-nucleotide insertion, which induced a frameshift during protein translation and introduced an early stop codon. This resulted in a nonsense mutation and the production of a truncated fbn1 protein(Fig. 3C). Finally, we generated F2 transgenic zebrafish by mating adult F1 *fbn1*$^{+/-}$ fish with Tg (kdrl: EGFP) and Tg (myl: EGFP) zebrafish. PCR analysis and sequencing verified that the randomly selected F2 *fbn1*$^{+/-}$heterozygous mutants carried the desired mutations. These results demonstrate the successful establishment of a transgenic line of *fbn1*$^{+/-}$ zebrafish, which can serve as a model for further genetic and functional studies on *fbn1* mutations.

F2 *fbn1*$^{+/-}$ zebrafish exhibit morphological, vascular, and cardiac defects

Then, we examined whether our transgenic zebrafish exhibit abnormal phenotypes of Marfan syndrome. Figure 4 demonstrates the morphological characteristics of F2 *fbn1*$^{+/-}$ zebrafish during the early stages of development (72 and 120 hpf). Compared to wild-type zebrafish, the F2 *fbn1*$^{+/-}$ zebrafish exhibited several key features of Marfan syndrome, including aortic arches bleeding, abnormal angiogenesis, decreased cardiac volume, cardiac function defects, and curly tail. The normal wild-type zebrafish showed minimal pericardial effusion and no tail defects. In contrast, moderately affected morphant exhibited a small amount of pericardial effusion, protruding mouth, and a curly tail; while severely affected morphants had large pericardial effusion, protruding mouth, and severe tail curvature (Fig. 4A). Notably, some F2 *fbn1*$^{+/-}$zebrafish exhibited aortic arch bleeding as early as 72 hpf. Cardiac function analysis, including measurements of fractional shortening (FS), ejection fraction (EF), and heart rate (HR), revealed abnormal systolic function and reduced cardiac volume in the F2 *fbn1*$^{+/-}$ zebrafish throughout development (Fig. 4B-C). Additionally, the F2 *fbn1*$^{+/-}$ zebrafish at 72 and 120 hpf displayed vascular defects, such as non-cavitated blood vessels, increased dorsal aorta diameter, and disordered intersegmental vasculature, compared to wild-type controls (Fig. 4D). Taken together, these findings suggest that the *fbn1*$^{+/-}$ zebrafish model the characteristic morphological, vascular, and cardiac abnormalities associated with Marfan syndrome, likely due to the p.Y2588* mutation in the *FBN1* gene.

The initial sample size for the F2 *fbn1*$^{+/-}$ zebrafish experimental group and WT control group was 120 individuals each. The experiment was repeated three times to ensure reliability of the results. The

overall death rate in F2 *fbn1*$^{+/-}$ group was about 4%. The abnormal angiogenesis phenotypes of F2 *fbn1*$^{+/-}$ and WT groups were quantitatively analyzed. The dorsal aorta diameters were measured and intersegmental vascular defects were assessed in both groups at 120 hpf. The results from the three experimental replicates demonstrated that the abnormal angiogenesis in the F2 group was significantly lower compared to the WT control group at 120 hpf ($p < 0.05$) (Fig. 4E).

F2 *fbn1*$^{+/-}$ zebrafish exhibits cartilage malformations

In WT zebrafish larvae, no alterations in cartilage and bone elements were observed. In contrast, F2 *fbn1*$^{+/-}$ zebrafish displayed enlarged Meckel's cartilage and an increased distance to the ceratohyal, indicative of a potential cartilage development defect associated with the p.Y2588* mutation in the *fbn1* gene (Fig. 4F-G). Furthermore, we employed a T-test to analyze the ratio of the distance from Meckel's cartilage (m) to the ceratohyal (ch) relative to head length in both F2 *fbn1*$^{+/-}$ and WT zebrafish. This analysis revealed that the ratio in the *fbn1*$^{+/-}$ group was significantly higher than that in the WT group ($p < 0.05$).

RNA-seq data revealed differentially expressed genes are predominantly associated with skeletal development and lipid metabolism

To elucidate the molecular pathways potentially implicated in MFS, we conducted a comprehensive transcriptional analysis utilizing RNA-seq. This analysis compared global gene expression profiles between untreated wild-type zebrafish larvae at 5 days post-fertilization and their *fbn1*$^{+/-}$ counterparts. Initially, we employed DESeq2 for a differential gene expression screen. The pairwise comparisons between the two groups revealed an identical number of differentially expressed genes (DEGs), totaling 27,309, comprising 25,522 known genes and 1,787 novel genes. Specifically, the comparison between WT and mutant (MU) zebrafish identified 5,157 DEGs. Among these, 1,900 genes were up-regulated, while 3,257 were down-regulated. The expression correlation, measured by Pearson's correlation coefficient (R2), was exceptionally high, ranging from 99.7 to 99.9% for the WT replicates (WT-1, WT-2, WT-3) and 98.9–99.2% for the MU replicates (MU-1, MU-2, MU-3). Principal Component Analysis (PCA) demonstrated a clustered distribution characteristic of the *fbn1*$^{+/-}$ group, suggesting a similarity in the underlying molecular composition among these samples (Fig. 5A-C). Volcano plots were utilized to visualize the extent of gene expression variation, highlighting significant DEGs involved in cardiovascular development, ossification, and lipid metabolism (Fig. 5D). A heatmap was employed to depict the expression patterns of these biologically relevant DEGs (Fig. 5E). An additional heatmap presented the comprehensive expression profiles of all DEGs between the WT and F2 *fbn1*$^{+/-}$ zebrafish (Fig. 5F). Collectively, these analyses confirmed the reliability of the sequencing data and established a foundation for subsequent investigative endeavors.

In our comprehensive RNA-sequencing analysis, a significant upregulation was observed for multiple genes associated with the leptin signaling pathway, including leptin receptor genes (*lepa* and *lepb*), as well as *fosl1a* and *fosl2*, which are known to play crucial roles in adipocyte differentiation and energy homeostasis. Conversely, a downregulation was noted for *irx5a*, *wnt11*, and *ctnnb1*, genes that are integral to the regulation of lipid metabolism (Table 1). Additionally, we identified an upregulation of *tgfb1a* and *tgfbr2a*, which are key components of the transforming growth factor-beta (TGF-β) signaling pathway, which in patients with Marfan syndrome, the TGF-β signaling pathway is typically upregulated (Fig. 6A).

RT-qPCR and Western blotting analysis identified the gene expression trends observed in RNA-Seq

To quantitatively assess the expression levels of the genes of interest, RT-qPCR was performed using specific primers for *lepa*, *lepb*, *fosl2*, *irx5a*, *wnt11*, *ctnnb1*, and *tgfb1a*. The relative expression levels were normalized to the housekeeping gene *gapdh*, which exhibited stable expression across all samples. The amplification efficiency of all primers was determined to be approximately equal, ensuring accurate comparison of expression levels. The RT-qPCR data revealed a significant up-regulation of *lepa*, *lepb*, and *fosl2* ($p < 0.05$), consistent with the RNA-Seq findings. Conversely, *irx5a*, *wnt11*, and *ctnnb1* exhibited a significant down-regulation ($p < 0.05$), aligning with the RNA-Seq results. Additionally, *tgfb1a* showed a significant increase in expression ($p < 0.05$), corroborating the high-throughput sequencing data (Fig. 6B). The WB analysis confirmed the upregulation of lepa, fosl1a, and fosl2 proteins, as evidenced by increased band intensities ($p < 0.05$). Similarly, a decrease in the protein levels of irx5a was observed ($p < 0.05$), supporting the gene expression trends observed in the RNA-Seq and RT-qPCR analyses (Fig. 6C).

Functional enrichment analysis suggested *fbn1* gene significantly influenced extracellular cellular functions

Subsequent to the identification of DEGs, we conducted enrichment analyses using the KEGG pathway database and the GO framework. The GO enrichment analysis highlighted significant enrichment of DEGs associated with the extracellular region, extracellular

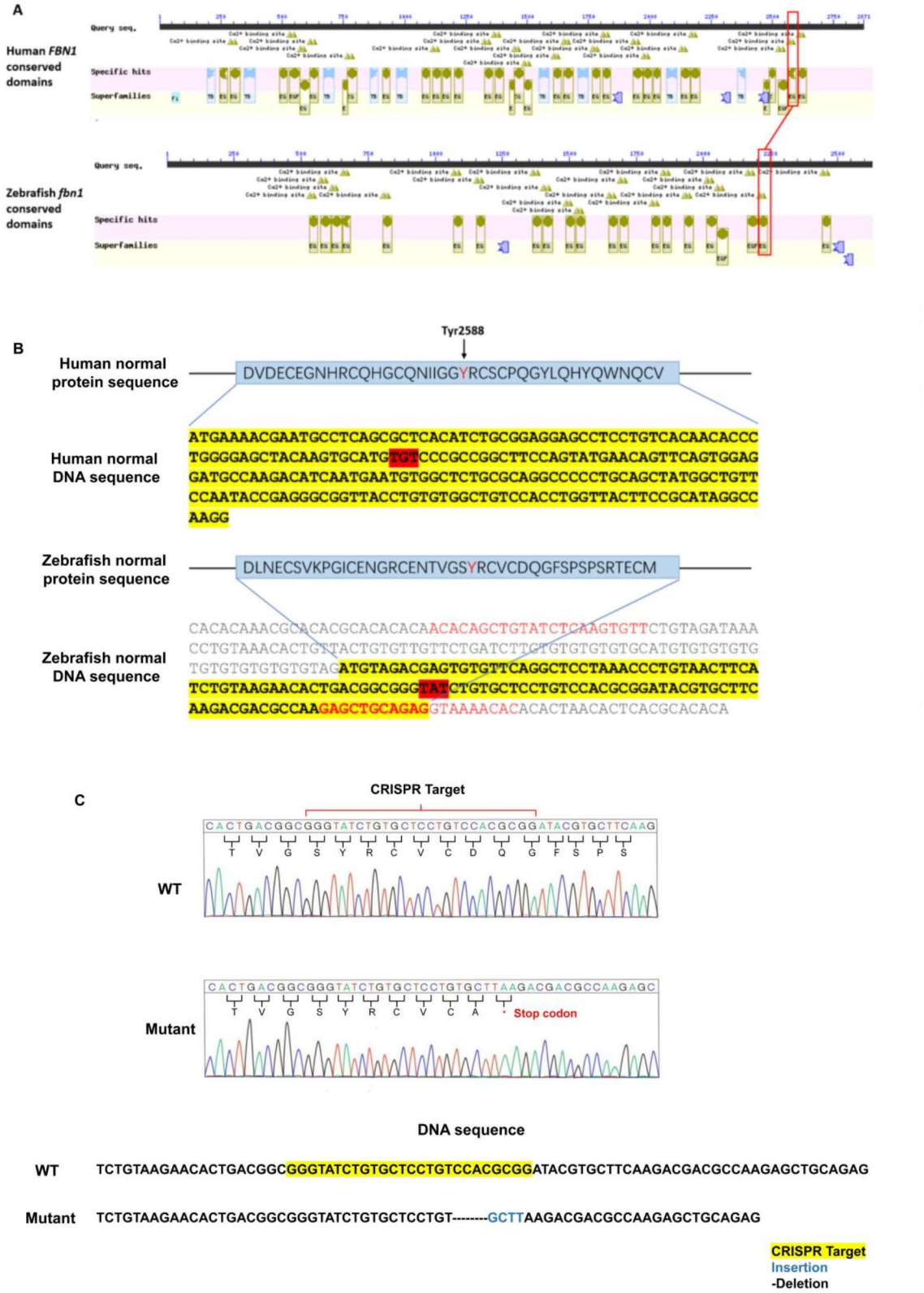

Fig. 3 Structure analyses of the nonsense mutation in the calcium binding (cb) epidermal growth factor (EGF)-like31 domain. (**A-B**) Generation of *fbn1*$^{+/-}$ zebrafish. The conserved domains of FBN1 protein in zebrafish are shown. The red box indicates the locus of the nonsense mutation, and the red highlight indicates the target of CRISPR/Cas9 gene editing. WT: wildtype. (**C**) Sequencing chromatograms of wild type and the mutant allele. The CRISPR/Cas9 induced the mutation containing a terminator insertion in *fbn1*

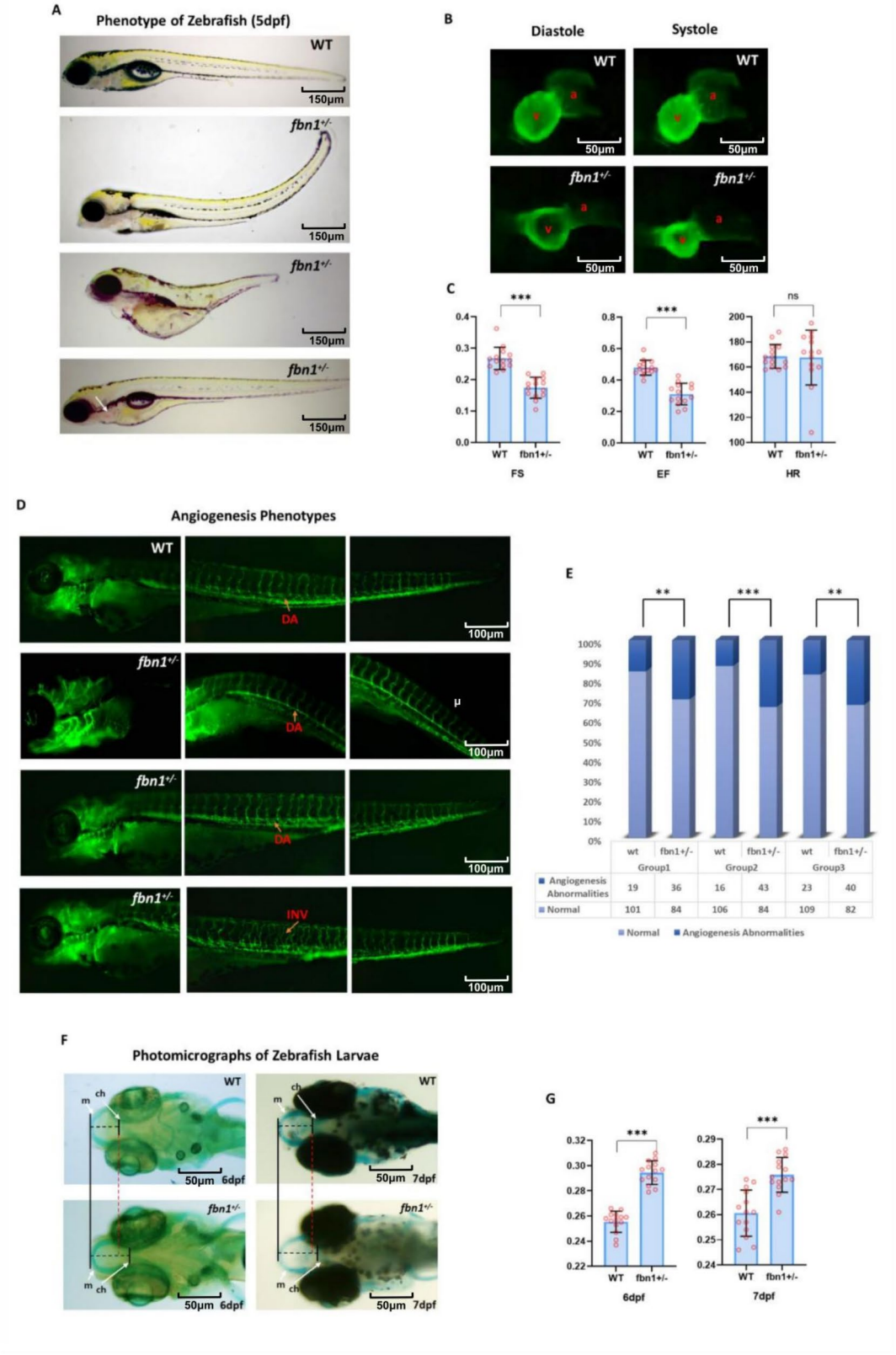

Fig. 4 (See legend on next page.)

(See figure on previous page.)

Fig. 4 Phenotypic Spectrum of F2 *fbn1*$^{+/-}$ Zebrafish larvae. F2 *fbn1*$^{+/-}$ Zebrafish were phenotyped with light microscopy in the zebrafish representative images are shown. Number of animals = 743, *N* = 3. Data were compared using an independent two-sample t-test, and the *P*-values were calculated to assess the significance of the difference in means between the two groups. Values of $*P \leq 0.05$ were considered significant. (**A**) Comparison of the morphology between F2 ***fbn1***$^{+/-}$ and WT zebrafish larvae at 72 hpf in the brightfield. WT zebrafish shows minimal pericardial effusion and no tail defects; A moderately affected morphant with a small amount of pericardial effusion, protruding mouth, and a curly tail; A severely affected morphant with a large pericardial effusion, protruding mouth, and severe tail curvature. The white arrow in the figure refers to the aortic arches bleeding (**B**) Comparison of the heart between F2 *fbn1*$^{+/-}$ and WT zebrafish larvae at 72 hpf. (**C**) Comparison of the cardiac function between F2 *fbn1*$^{+/-}$ and WT zebrafish larvae at 72 hpf. F2 *fbn1*$^{+/-}$ zebrafish appear significant defects in ejection fraction and fraction shorting. (**D**) F2 *fbn1*$^{+/-}$ Zebrafish larvae show angiogenesis abnormalities phenotype. WT zebrafish phenotype (120 hpf). F2 *fbn1*$^{+/-}$ Zebrafish shows the blood vessels are not cavitated. Some F2 *fbn1*$^{+/-}$ Zebrafish shows the increased dorsal aorta diameter phenotype and intersegmental vascular disorders. (**E**) Incidence of angiogenesis abnormalities in F2 *fbn1*$^{+/-}$ Zebrafish larvae at 120 hpf. hpf: hours post-fertilization; FS: fraction shorting; EF: ejection fraction. (**F**). Photomicrographs of 144 and 168 hpf zebrafish larvae at the ventral view. All cartilage and bones appear normally shaped and developed in WT zebrafish. F2 *fbn1*$^{+/-}$ zebrafish exhibits bigger Meckel's cartilage and the increased distance from Meckel's cartilage to the ceratohyal increased. (**G**). The ratio of the distance from Meckel's cartilage to ceratohyal and the length of head in F2 *fbn1*$^{+/-}$ and WT zebrafish. N: number of independent experiments; WT: wild type; hpf: hour post fertilization; ns: no sense; **: $p < 0.01$; ***: $p < 0.001$

space, external encapsulating structures, and extracellular matrix, suggesting that the *fbn1* gene significantly influences extracellular cellular functions (Fig. 7A-B).

Employing the hierarchical classification system of the KEGG database, we tallied the pathways and their constituent genes that were enriched. Our findings from the top 20 KEGG enrichments revealed a substantial enrichment of DEGs in pathways linked to retinol metabolism and modified cell adhesion, extracellular matrix (ECM)-receptor interaction, and focal adhesion. These observations suggest that the fbn1 mutation's mechanism potentially disrupts adipose tissue homeostasis and induces pathological changes in blood vessels, particularly through pathways interconnected with endocrine and signal transduction systems (Fig. 7C-D).

Discussion

Since the *FBN1* gene was identified as the causative agent of MFS, a total of 6,633 variants have been documented in the most comprehensive FBN1 mutation database to date [9]. Variations are found throughout the entire length of the gene, with 1,919 of pathogenic and 1,309 of likely pathogenic. Single-gene mutations consist of 93.4% of all variations. In our study, we recruited a family exhibiting the MFS phenotype from Southern China and discovered a novel *FBN1* variant, [NM_000138.5; c.7764 C > G: p.(Y2588*)], which, to our knowledge, has not been previously reported in the existing literature. A similar nonsense variant (rs1555394144; FBN1 Q2594*) is reported in ClinVar. This nonsense variant results in a premature stop codon, leading to a truncated protein. This mechanism, similar to the novel variant Y2588*, which is associated with Marfan syndrome and related disorders. The variant reported in ClinVar also provides further evidence supporting the pathogenicity of the variant Y2588*.

The *FBN1* gene is widely expressed across various human tissues, encompassing cartilage, tendons, the cornea, ocular zonules, and the cardiovascular system [13]. As annotated in the Kyoto Encyclopedia of Genes and Genomes (KEGG), the FBN1 protein participates in the TGF-β signaling pathway, specifically within the hsa04350 pathway. Beyond its structural functions, fibrillin microfibrils play a role in maintaining tissue homeostasis by interacting with cell surface receptors like integrins and with growth factors, including TGF-β and bone morphogenetic proteins (BMPs) [14, 15]. Elevated levels of active TGF-β, resulting from diminished fibrillin, have been associated with the pathogenesis of MFS in mice with fibrillin-1 deficiencies. The most prominent features observed in these mice, as well as in MFS patients with heterozygous *FBN1* mutations, include lung emphysema, vascular complications, and excessive bone growth [16].

A very similar mutation of NM_000138.5(*FBN1*): c.7763 A > G (p.Y2588C) to our study was reported with uncertain significance in MFS (https://www.ncbi.nlm.nih.gov/clinvar/variation/571222/). In this particular mutation, the tyrosine residue at codon 2588 is replaced with cysteine, an amino acid with significantly different characteristics, within the cbEGF-like domain. The majority of *FBN1* mutations identified to date have involved either the substitution or the introduction of cysteine residues within these cbEGF domains [17]. This amino acid position is highly conserved in available vertebrate species, this alteration is predicted to be deleterious by in silico analysis. Furthermore, based on internal structural assessment, this alteration disrupts proper disulfide-mediated folding of cbEGF domain 41 [18] and is likely to be pathogenic. However, Keith et al. pointed out that the available evidence was currently insufficient to determine the role of this variant in the disease. Therefore, it has been classified as a variant of uncertain significance [19]. Faivre et al. found that missense mutations of *FBN1* eliminating a cysteine had a higher probability of resulting in disease than mutations creating a cysteine [20]. Mutations leading to a premature termination

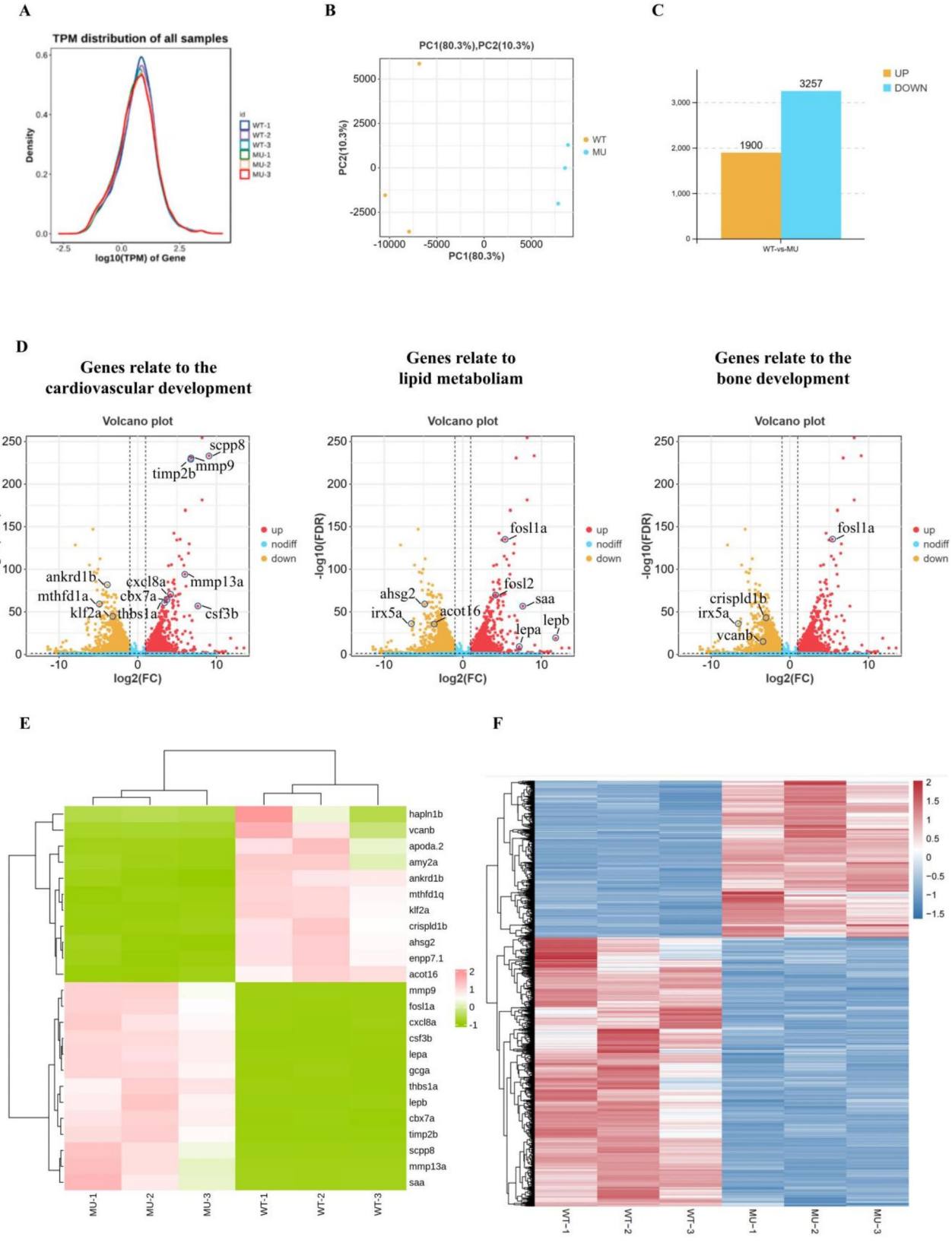

Fig. 5 (See legend on next page.)

(See figure on previous page.)

Fig. 5 Whole transcriptome RNA-seq profile of larval zebrafish. (**A**) Gene expression abundance distribution plot. Tthe horizontal axis depicts the log10-transformed transcripts per million (tpm), signifying higher expression levels at greater values. The vertical axis represents gene abundance, defined as the proportion of genes at a given expression level relative to the total number of detected expressed genes. Each color in the plot corresponds to a distinct sample, with the distribution curve's peak highlighting the most concentrated region of gene expression across the samples. (**B**) Principal Component Analysis. The coordinates along the first principal component (PC1) are shown, accompanied by the percentage in parentheses that denotes PC1's contribution to sample variability. Similarly, the second principal component (PC2) is represented, with its contribution to sample differences indicated. The plot's colored dots correspond to individual samples, visually demonstrating their relationships in the multivariate space. (**C**) Differential gene expression plot. Horizontal axis: Paired comparison samples; Vertical axis: Number of differentially expressed genes. (**D**) Differential gene expression volcano plot. In the volcano plot, significant genes involved in cardiovascular development, ossification, and fluid metabolism are specifically marked, indicating their role in the biological processes of interest. (**E**). Heatmap of expression of these significant differential genes that are marked in the volcano plot. (**F**). Heatmap of expression of differential genes in the WT and F2 *fbn1*$^{+/-}$ zebrafish. The heatmap summarizing the expression profiles of all differentially expressed genes between the wild-type and F2 heterozygous fbn1+/– zebrafish, providing an overview of the genetic differences that may underlie phenotypic variations

codon (PTC), namely nonsense and frameshift mutations, were plotted against cysteine mutations to determine if the latter were more frequently associated with major manifestations at the cardiovascular level [21].

This newly identified alteration [NM_000138.5; c.7764 C > G: p.(Y2588*)] in *FBN1*, as discovered in our study, is anticipated to lead to loss of function through premature protein truncation or nonsense-mediated mRNA decay, and is interpreted as a mutation causing the disease. In zebrafish, we identified functional evidence of the detected nonsense mutation, which aligns with the clinical significance suggesting a pathogenic or likely pathogenic nature indicated in all 427 known nonsense variants of *FBN1* [22]. The EGF-like domain truncation resulting from *fbn1*$^{+/-}$ mutation in our study caused noticeable aortic arches bleeding, abnormal angiogenesis, decreased cardiac volume, cardiac function defects, and morphological defects in zebrafish larvae, reminiscent of human MFS and other *fbn1*$^{+/-}$ models [23, 24]. We also found that this nonsense variant led to a more loosely arranged and structurally abnormal conformation prior to the premature termination, which may further impair the function of the protein.

Clinical evidence showed that certain variants in the PTC of *FBN1* and the neonatal region (exons 25–33) are independently significant predictors of severe scoliosis development [25, 26]. In our investigation, scoliosis was observed in the proband as well as her daughter and son, and this was confirmed using a zebrafish model, in which the *fbn1*$^{+/-}$ zebrafish exhibited severe tail curvature and abnormal Meckel's cartilage. Measurements of the ratio between Meckel's cartilage and head length were higher in the *fbn1*$^{+/-}$ zebrafish compared to wild-type. We demonstrated that this genetic variation is responsible for the onset of severe scoliosis in individuals with Marfan syndrome. Patients carrying this particular pathogenic *fbn1* variant should be closely monitored for progression of scoliosis [26].

RNA-seq analysis revealed that genes associated with the TGF-β signaling pathway were upregulated in *fbn1*$^{+/-}$ zebrafish. This is consistent with the fact that alterations in *fbn1* gene result in loss-of-function of fbn1, which leads to liberation on TGF-β, and the subsequent activation of Smad-mediated gene expression. the activated TGF-β promotes Smad-mediated gene expression [27, 28]. TGF-β signaling regulates a wide variety of cellular processes in many different cell types, and its effects are context-dependent. The upregulation of the TGF-β pathway has been shown to promote the occurrence of thoracic aortic aneurysms (TAA) and skeletal abnormalities in patients with MFS [29, 30]. The analysis did show decreased expression of the *irx5a* gene and increased expression of *fosl1a* and *fosl2* genes, all of which have been implicated in bone development [29].

Table 1 Expression of lipid metabolism-related genes in the WTgroup and *fbn1*$^{+/-}$ group

Gene	WT-1	WT-2	WT-3	WT-mean	MU-1	MU-2	MU-2	MU-mean	*P*value
fosl1a	3.326	1.93	3.037	2.764	130.99	125.907	90.316	115.7	0.000910
lepb	0	0	0.124	0.041	134.995	180.088	127.848	147.6	0.000835
lepa	0.169	0.144	0	0.104	16.229	15.11	13.426	14.92	0.000054
fosl2	5.802	6.204	4.436	5.481	30.738	32.329	36.919	33.33	0.000134
irx5a	32.729	32.24	26.407	30.46	17.608	18.401	22.11	19.37	0.010763
wnt11	42.957	43.844	37.41	41.40	11.916	11.503	13.283	12.23	0.000151
ctnnb1	11.916	11.503	13.283	12.23	173.509	188.357	180.502	180.8	0.000003
tgfb1a	4.122	4.483	4.245	4.283	18.109	18.215	16.167	17.50	0.000040
tgfbr2a	1.31	1.267	0.903	1.160	9.862	12.931	8.457	10.42	0.002223

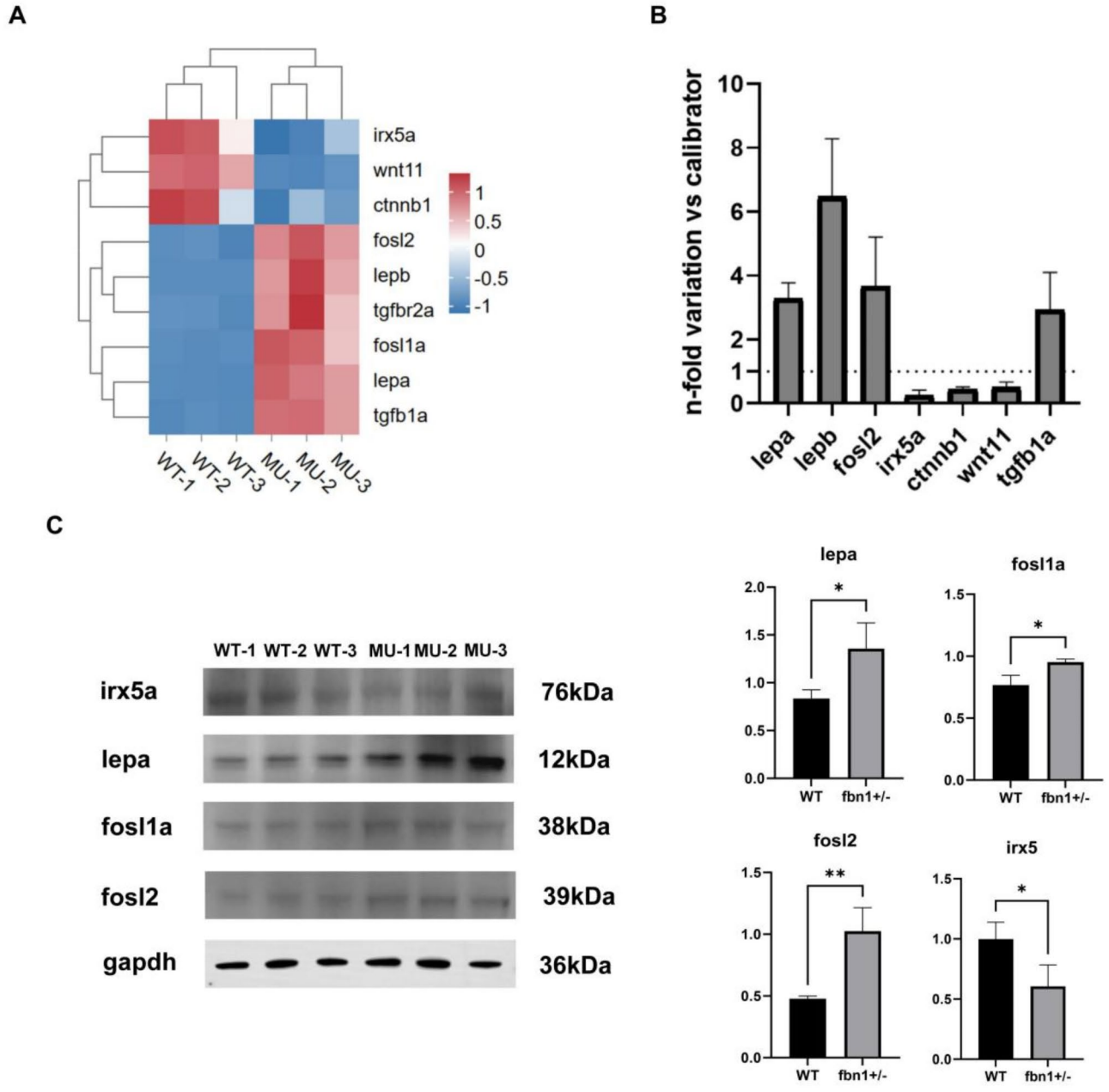

Fig. 6 (**A**). Heatmap of expression of these significant differential genes that related to bone development and lipid metabolism. (**B**) qRT-PCR. The bar graph shows expression of *lepa*, *lepb*, *fosl2*, *irx5a*, *ctnnb1*, *wnt11*, and *tgfb1*a mRNA in *fbn1*$^{+/-}$ zebrafish. The results were obtained using 10 zebrafish per each experimental group and are expressed as mean ± SEM. Data were compared using an independent two-sample t-test, and the *P*-values were calculated to assess the significance of the difference in means between the two groups. Values of *$P \leq 0.05$ were considered significant. (**C**). Western blotting analysis. Proteins related to lipid metabolism were detected by western blotting for their presence and quantity. *: $p < 0.05$; **: $p < 0.01$; ***: $p < 0.001$. Full-length blots/gels are presented in Supplementary Fig. 1

Interestingly, these bone development-related genes (*irx5a*, *fosl1a*, and *fosl2*) are also involved in lipid metabolism, along with increased expression of *lepa and lepb.* Individuals with MFS frequently develop type 2 diabetes (T2DM) and exhibit a lipodystrophic phenotype characterized by very low overall body fat levels [31, 32]. The human homolog of *irx5a*, known as IRX5, has been shown to promote adipogenesis, repress glycolysis, and elevate leptin expression in human adipocytes [33]. Additionally, adipocyte-specific *Fosl2*-knockout mice demonstrated a significant reduction in serum leptin levels [34]. Downregulation of the IRX5 gene has been shown to reduce body weight and white adipose tissue (WAT) mass in both mice and humans through a combination of cell-autonomous mechanisms and sympathetic nervous

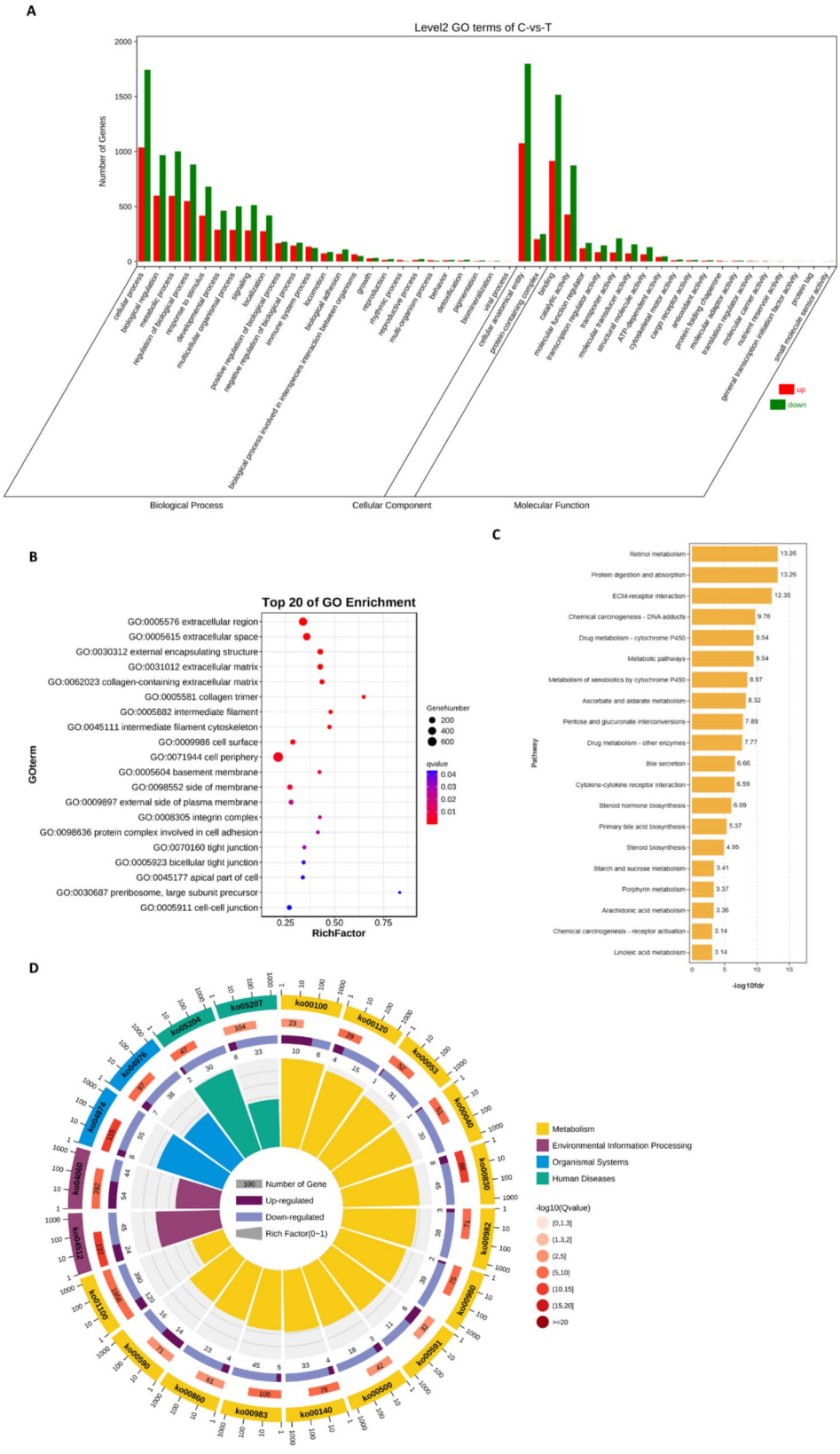

Fig. 7 (See legend on next page.)

(See figure on previous page.)

Fig. 7 Differential gene expression analysis. (**A**) The bar chart of GO enrichment analysis. The x-axis represents the second-level GO terms, the y-axis represents the number of differentially expressed genes in that term, with red indicating upregulation and green indicating downregulation. (**B**) bubble diagram of the top 15 noticeably enriched pathways. The graph is plotted with *p*-values of significance for various pathways. The abscissa denotes the gene-rich factor (i.e., the number of differential genes enriched to the current pathway/the number of that species enriched to the current pathway), and the ordinate represents the pathway. Bubble size represents the number of genes enriched in different pathways, and bubble color represents the degree of enrichment in different pathways. (**C**) statistical plot of the grade B classification of each pathway of the differentially enriched genes. (**D**) circle-marker plots of the top 15 significantly enriched differential pathways. Outside the circle is a sitting ruler of the gene number. Different colors represent different KEGG A Class

system-induced changes [35]. Furthermore, the down-regulation of *IRX5* also can increase the expression and function of leptin in the hypothalamus by modulating the number and function of neurons sensitive to leptin signaling, thereby potentially affecting food intake and energy expenditure [36].

However, the specific mechanisms underlying the relationship between lipid metabolism and the role of IRX5 and leptin require further research for detailed elucidation. Patients with MFS should be monitored not only for cardiovascular system complications but also for metabolic disturbances, as the disease appears to have a significant impact on lipid metabolism and associated pathways.

Overall, MFS serves as a proof-of-concept clinical challenge with unmet needs in both diagnosis and treatment. Despite the extensive research have conducted on the function of *FBN1*, our study has contributed novel insights to the overall understanding of *FBN1*. Accurate diagnosis of MFS is particularly important, which relies on the detection of deleterious mutations in the *FBN1* gene, alongside the identification of syndromic symptoms. However, genetic testing often reveals *FBN1* variants that are not conclusively linked to disease pathogenesis [37].

Another objective of our study is to develop a zebrafish-based model that facilitates the rapid classification of unknown variants in the *FBN1* gene, thereby aiding in MFS diagnosis [38]. Additionally, this model will enable efficient screening of drug libraries to identify potential new therapies, potentially leading to the discovery of patient-specific treatments. Zebrafish as an innovative and efficient tool to enhance the clinical diagnosis and treatment of MFS is possible on the horizon.

Abbreviations

MFS	Marfan syndrome
FBN1	Fibrillin-1
MU	Mutant
WT	Wild type
EGF	Epidermal growth factor
hpf	Hours post-fertilization
FS	Fractional shortening
EF	Ejection fraction
HR	Heart rate
DEG	Differentially expressed genes
PCA	Principal Component Analysis
ECM	Extracellular matrix
KEGG	Kyoto Encyclopedia of Genes and Genomes
BMPs	Bone morphogenetic
PTC	Proteins premature termination codon
TAA	Thoracic aortic aneurysms
T2DM	Type 2 diabetes
WAT	White adipose tissue

Supplementary Information

The online version contains supplementary material available at https://doi.org/10.1186/s12864-025-11471-7.

Supplementary Material 1

Acknowledgements

This work was supported by National Natural Science Foundation of China (Grant Number: 82270308); National Key Research and Development Program of China (Grant Number: 2023ZD0504405-1); Foshan Nanhai District's 14th Five-Year Plan for Key Medical Specialties Construction Project (No. 20).

Author contributions

All authors contributed to the study conception and design. Material preparation, data collection and analysis were performed by SH, JC, QW, RZ, RH, CY, HZ and MF. The funders were provided by LL. The first draft of the manuscript was written by SH. LL, HZ, and JZ commented on previous versions of the manuscript. All authors read and approved the final manuscript.

Funding

This work was supported by National Natural Science Foundation of China (Grant Number: 82270308); National Key Research and Development Program of China (Grant Number: 2023ZD0504405-1); Foshan Nanhai District's 14th Five-Year Plan for Key Medical Specialties Construction Project (No. 20).

Data availability

No datasets were generated or analysed during the current study.

Declarations

Ethics approval and consent to participate

All procedures performed in studies involving human participants were in accordance with the ethical standards of the institutional and/or national research committee and with the 1964 Helsinki declaration and its later amendments or comparable ethical standards. Informed consent was obtained from all individual participants included in the study. All animal experiments were conducted in accordance with the guidelines of the Guangdong Provincial People's Hospital Animal Care and Use Committee and were approved under the ethical approval number KY2023-519-02. The guidelines from Directive 2010/63/EU of the European Parliament on the protection of animals used for scientific purposes and the NIH Guide for the Care and Use of Laboratory Animals were strictly followed to ensure the welfare of the animals.

Consent for publication

Informed consent was obtained from all individual participants included in the study. The authors affirm that human research participants provided informed consent for publication of the images in Figure(s) 1a, and 1b.

Competing interests

The authors declare no competing interests.

Received: 10 December 2024 / Accepted: 11 March 2025
Published online: 24 March 2025

References

1. Keane MG, Pyeritz RE. Medical management of Marfan syndrome. Circulation. 2008;117(21):2802-13. PubMed PMID: 18506019. https://doi.org/10.1161/circulationaha.107.693523
2. Sakai LY, Keene DR, Renard M, De Backer J. FBN1: the disease-causing gene for Marfan syndrome and other genetic disorders. Gene. 2016;591(1):279–91. https://doi.org/10.1016/j.gene.2016.07.033. Epub 20160718.
3. Arnaud P, Milleron O, Hanna N, Ropers J, Ould Ouali N, Affoune A, et al. Clinical relevance of genotype-phenotype correlations beyond vascular events in a cohort study of 1500 Marfan syndrome patients with FBN1 pathogenic variants. Genet Med. 2021;23(7):1296–304. https://doi.org/10.1038/s41436-021-01132-x. Epub 20210317.
4. Milleron O, Arnoult F, Delorme G, Detaint D, Pellenc Q, Raffoul R, et al. Pathogenic FBN1 genetic variation and aortic dissection in patients with Marfan syndrome. J Am Coll Cardiol. 2020;75(8):843–53. PubMed PMID: 32130918. https://doi.org/10.1016/j.jacc.2019.12.043
5. Barman A, Deb B, Chakraborty S. A glance at genome editing with CRISPR-Cas9 technology. Curr Genet. 2020;66(3):447–62. https://doi.org/10.1007/s00294-019-01040-3. Epub 20191105.
6. Saber Sichani A, Ranjbar M, Baneshi M, Torabi Zadeh F, Fallahi J. A review on advanced CRISPR-Based Genome-Editing tools: base editing and prime editing. Mol Biotechnol. 2023;65(6):849–60. https://doi.org/10.1007/s12033-022-00639-1. Epub 20221222.
7. Jumper J, Evans R, Pritzel A, Green T, Figurnov M, Ronneberger O, et al. Highly accurate protein structure prediction with alphafold. Nature. 2021;596(7873):583–9. https://doi.org/10.1038/s41586-021-03819-2. Epub 20210715.
8. Richards S, Aziz N, Bale S, Bick D, Das S, Gastier-Foster J, et al. Standards and guidelines for the interpretation of sequence variants: a joint consensus recommendation of the American college of medical genetics and genomics and the association for molecular pathology. Genet Med. 2015;17(5):405–24. https://doi.org/10.1038/gim.2015.30. Epub 20150305.
9. Available from: https://www.uniprot.org/uniprotkb/P35555/entry
10. Bouzeghrane F, Reinhardt DP, Reudelhuber TL, Thibault G. Enhanced expression of fibrillin-1, a constituent of the myocardial extracellular matrix in fibrosis. Am J Physiol Heart Circ Physiol. 2005;289(3):H982–91. https://doi.org/10.1152/ajpheart.00151.2005. Epub 20050422.
11. Yin R, Pierce BG. Evaluation of alphafold antibody-antigen modeling with implications for improving predictive accuracy. Protein Sci. 2024;33(1):e4865.: 10.1002/pro.4865. PubMed PMID: 38073135; PubMed Central PMCID: PMCPMC10751731.
12. Siegert AM, Serra-Peinado C, Gutiérrez-Martínez E, Rodríguez-Pascual F, Fabregat I, Egea G. Altered TGF-β endocytic trafficking contributes to the increased signaling in Marfan syndrome. Biochim Biophys Acta Mol Basis Dis. 2018;1864(2):554–62. PubMed PMID: 29174139.
13. Milewicz DM, Braverman AC, De Backer J, Morris SA, Boileau C, Maumenee IH, et al. Marfan syndrome. Nat Rev Dis Primers. 2021;7(1):64. https://doi.org/10.1038/s41572-021-00298-7. Epub 20210902.
14. Du Q, Zhang D, Zhuang Y, Xia Q, Wen T, Jia H. The molecular genetics of Marfan syndrome. Int J Med Sci. 2021;18(13):2752–66. Epub 20210527. PubMed PMID: 34220303; PubMed Central PMCID: PMCPMC8241768. https://doi.org/10.7150/ijms.60685
15. Sun L, Chang Y, Jiang P, Ma Y, Yuan Q, Ma X. Association of gene polymorphisms in FBN1 and TGF-β signaling with the susceptibility and prognostic outcomes of Stanford type B aortic dissection. BMC Med Genomics. 2022;15(1):65. https://doi.org/10.1186/s12920-022-01213-z. Epub 20220320.
16. Franken R, Groenink M, de Waard V, Feenstra HM, Scholte AJ, van den Berg MP, et al. Genotype impacts survival in Marfan syndrome. Eur Heart J. 2016;37(43):3285–90. https://doi.org/10.1093/eurheartj/ehv739. Epub 20160118.
17. Vollbrandt T, Tiedemann K, El-Hallous E, Lin G, Brinckmann J, John H, et al. Consequences of cysteine mutations in calcium-binding epidermal growth factor modules of fibrillin-1. J Biol Chem. 2004;279(31):32924–31. https://doi.org/10.1074/jbc.M405239200. Epub 20040525.
18. Jensen SA, Iqbal S, Lowe ED, Redfield C, Handford PA. Structure and interdomain interactions of a hybrid domain: a disulphide-rich module of the fibrillin/ltbp superfamily of matrix proteins. Structure. 2009;17(5):759–68. PubMed PMID: 19446531; PubMed Central PMCID: PMCPMC2724076. https://doi.org/10.1016/j.str.2009.03.014
19. Nykamp K, Anderson M, Powers M, Garcia J, Herrera B, Ho YY, et al. Sherloc: a comprehensive refinement of the ACMG-AMP variant classification criteria. Genet Med. 2017;19(10):1105–17. https://doi.org/10.1038/gim.2017.37. Epub 20170511.
20. Collod-Béroud G, Le Bourdelles S, Ades L, Ala-Kokko L, Booms P, Boxer M, et al. Update of the UMD-FBN1 mutation database and creation of an FBN1 polymorphism database. Hum Mutat. 2003;22(3):199–208. PubMed PMID: 12938084. https://doi.org/10.1002/humu.10249
21. Gao L, Tian T, Zhou X, Fan L, Wang R, Wu H. Detection of ten novel FBN1 mutations in Chinese patients with typical or incomplete Marfan syndrome and an overview of the genotype-phenotype correlations. Int J Cardiol. 2019;293:186–91. https://doi.org/10.1016/j.ijcard.2019.06.066. Epub 20190628.
22. Martins-Dias P, Romão L. Nonsense suppression therapies in human genetic diseases. Cell Mol Life Sci. 2021;78(10):4677–701. https://doi.org/10.1007/s00018-021-03809-7. Epub 20210322.
23. Prendergast A, Ziganshin BA, Papanikolaou D, Zafar MA, Nicoli S, Mukherjee S et al. Phenotyping Zebrafish Mutant Models to Assess Candidate Genes Associated with Aortic Aneurysm. Genes (Basel). 2022;13(1). Epub 20220110. PubMed PMID: 35052463; PubMed Central PMCID: PMCPMC8775119. https://doi.org/10.3390/genes13010123
24. Yin X, Hao J, Yao Y. CRISPR/Cas9 in zebrafish: an attractive model for FBN1 genetic defects in humans. Mol Genet Genomic Med. 2021;9(10):e1775. https://doi.org/10.1002/mgg3.1775. Epub 20210729.
25. Takeda N, Inuzuka R, Maemura S, Morita H, Nawata K, Fujita D, et al. Impact of pathogenic FBN1 variant types on the progression of aortic disease in patients with Marfan syndrome. Circ Genom Precis Med. 2018;11(6):e002058. PubMed PMID: 29848614. https://doi.org/10.1161/circgen.117.002058
26. Taniguchi Y, Takeda N, Inuzuka R, Matsubayashi Y, Kato S, Doi T, et al. Impact of pathogenic FBN1 variant types on the development of severe scoliosis in patients with Marfan syndrome. J Med Genet. 2023;60(1):74–80. https://doi.org/10.1136/jmedgenet-2021-108186. Epub 20211216.
27. Dai C, Rennhack JP, Arnoff TE, Thaker M, Younger ST, Doench JG, et al. SMAD4 represses FOSL1 expression and pancreatic cancer metastatic colonization. Cell Rep. 2021;36(4):109443. PubMed PMID: 34320363; PubMed Central PMCID: PMCPMC8350598. https://doi.org/10.1016/j.celrep.2021.109443
28. Li L, Huang J, Liu Y. The extracellular matrix glycoprotein fibrillin-1 in health and disease. Front Cell Dev Biol. 2023;11:1302285. Epub 20240110. PubMed PMID: 38269088; PubMed Central PMCID: PMCPMC10806136. https://doi.org/10.3389/fcell.2023.1302285
29. Bai M, Han Y, Wu Y, Liao J, Li L, Wang L, et al. Targeted genetic screening in mice through haploid embryonic stem cells identifies critical genes in bone development. PLoS Biol. 2019;17(7):e3000350. https://doi.org/10.1371/journal.pbio.3000350. Epub 20190702.
30. Tae HJ, Petrashevskaya N, Marshall S, Krawczyk M, Talan M. Cardiac remodeling in the mouse model of Marfan syndrome develops into two distinctive phenotypes. Am J Physiol Heart Circ Physiol. 2016;310(2):H290–9. https://doi.org/10.1152/ajpheart.00354.2015. Epub 20151113.
31. Tiedemann K, Muthu ML, Reinhardt DP, Komarova SV. Male Marfan mice are predisposed to high-fat diet-induced obesity, diabetes, and fatty liver. Am J Physiol Cell Physiol. 2022;323(2):C354–66. https://doi.org/10.1152/ajpcell.00062.2022. Epub 20220627.
32. Le Y, Zhang J, Hong T, Yang J. Coexistence of type 2 diabetes mellitus, arginine vasopressin deficiency, and Marfan syndrome: A case report. J Diabetes Investig. 2024;15(7):964–7. https://doi.org/10.1111/jdi.14169. Epub 20240302.
33. Jiang B, Huang L, Tian T, Wu H, Yao H, Marmo T, et al. IRX5 promotes adipogenesis of hMSCs by repressing Glycolysis. Cell Death Discov. 2022;8(1):204. https://doi.org/10.1038/s41420-022-00986-7. Epub 20220415.
34. Drosos I, Chalikias G, Pavlaki M, Kareli D, Epitropou G, Bougioukas G, et al. Differences between perivascular adipose tissue surrounding the heart and the internal mammary artery: possible role for the leptin-inflammation-fibrosis-hypoxia axis. Clin Res Cardiol. 2016;105(11):887–900. https://doi.org/10.1007/s00392-016-0996-7. Epub 20160623.
35. Bjune JI, Dyer L, Røsland GV, Tronstad KJ, Njølstad PR, Sagen JV, et al. The homeobox factor Irx3 maintains adipogenic identity. Metabolism. 2020;103:154014. https://doi.org/10.1016/j.metabol.2019.154014. Epub 20191118.
36. Zhou Y, Du X, Chen C, Shi B, Chen K. Marfan syndrome with type 2 diabetes mellitus: A case report from China. Med (Baltim). 2019;98(3):e14176. PubMed

PMID: 30653163; PubMed Central PMCID: PMCPMC6370063. https://doi.org/10.1097/md.0000000000014176

37. Oller J, Gabandé-Rodríguez E, Ruiz-Rodríguez MJ, Desdín-Micó G, Aranda JF, Rodrigues-Diez R, et al. Extracellular tuning of mitochondrial respiration leads to aortic aneurysm. Circulation. 2021;143(21):2091–109. https://doi.org/10.1161/circulationaha.120.051171. Epub 20210312.
38. Ng B, Xie C, Su L, Kuthubudeen FF, Kwek XY, Yeong D, et al. IL11 (Interleukin-11) causes emphysematous lung disease in a mouse model of Marfan syndrome. Arterioscler Thromb Vasc Biol. 2023;43(5):739–54. https://doi.org/10.1161/atvbaha.122.318802. Epub 20230316.

Publisher's note